RSC Advances

PAPER

View Article Online
View Journal | View Issue

Cite this: *RSC Adv.*, 2026, **16**, 22269

Selenium-activated monolithic FeNi layered double hydroxide electrodes: binder-free, self-supported architectures for durable alkaline oxygen evolution

Alaa Hassan,[ab] Ghada E. Khedr,[c] Aya K. Gomaa,[a] Laila H. Abdel-Rahman,[b] Hussein M. El-Sagher[b] and Nageh K. Allam *[a]

Received 19th March 2026
Accepted 21st April 2026

DOI: 10.1039/d6ra02304e

rsc.li/rsc-advances

Developing earth-abundant, durable, and scalable oxygen evolution electrocatalysts is critical for alkaline water electrolysis. Herein, a monolithic, binder-free Se-activated FeNi layered double hydroxide (Se–FeNi-LDH) electrode grown directly on an ultrathin FeNi alloy substrate is introduced. This integrated architecture eliminates polymeric binders and interfacial resistance, enabling efficient electron/mass transport under industrial conditions. The optimized FeNi-LDH1-Se_{05} electrode delivers outstanding OER activity with overpotentials of only 240 and 290 mV at 10 and 100 mA cm^{-2}, respectively, a low Tafel slope of 37 mV dec^{-1}, and stable operation for 120 h at 100 mA cm^{-2}. In a practical electrolyzer (Se–FeNi-LDH||Pt), a cell voltage of 1.56 V at 10 mA cm^{-2} is achieved. Selenium incorporation modulates the electronic structure of Fe/Ni centers, enhances active surface area and charge-transfer kinetics, and maintains high faradaic efficiency (~97.5%). This work establishes selenium activation in a binder-free monolithic LDH platform as a scalable, mechanically robust strategy for high-performance alkaline OER.

1 Introduction

Since the industrial revolution, fossil fuels have dominated the global energy landscape, underpinning unprecedented industrial growth and technological advancement.[1,2] However, the continued and intensive exploitation of these nonrenewable resources has resulted in profound environmental consequences, including greenhouse gas emissions, climate change, and ecological degradation, alongside the inevitable depletion of finite reserves. As a result, the global energy system is increasingly strained, highlighting an urgent need for sustainable and renewable alternatives that can alleviate dependence on conventional fossil-fuel-based energy infrastructures.

Hydrogen has emerged as one of the most promising energy carriers for a sustainable energy future owing to its high gravimetric energy density, carbon-free combustion, and recyclability.[1,3,4] When produced from renewable sources, hydrogen offers a viable pathway toward decarbonizing energy-intensive sectors. Among the available hydrogen production technologies, electrochemical water splitting stands out as a clean and efficient approach, as it directly converts electrical energy into chemical energy without generating greenhouse gas emissions.[5–8] In alkaline media, water electrolysis involves two coupled half-reactions: the oxygen evolution reaction (OER, $4OH^- \rightarrow O_2 + 2H_2O + 4e^-$) at the anode and the hydrogen evolution reaction (HER, $2H_2O + 2e^- \rightarrow H_2 + 2OH^-$) at the cathode.[9–11] Thermodynamically, the OER requires a potential of 1.23 V *versus* the reversible hydrogen electrode (RHE) under standard conditions (25 °C, 1 atm), whereas the HER proceeds at 0 V *versus* RHE.[12] In practice, however, additional energy input in the form of overpotential (η) is required to overcome kinetic barriers.

Notably, the OER is a complex, multistep proton-coupled electron transfer process involving the formation of oxygen–oxygen bonds, which renders its reaction kinetics intrinsically sluggish. Consequently, the OER typically demands large overpotentials and is widely recognized as the principal kinetic bottleneck in overall water electrolysis. To date, the most efficient OER electrocatalysts are based on precious metals, particularly IrO_2 and RuO_2, while platinum-based materials dominate HER catalysis. Despite their superior activity, the scarcity, high cost, and limited long-term sustainability of those metals severely restrict their widespread and commercial deployment. Therefore, developing cost-effective, earth-abundant, and durable electrocatalysts capable of delivering high OER performance remains a central challenge in the field of electrochemical energy conversion.[12]

In response to this challenge, extensive efforts have been devoted to exploring non-noble-metal-based OER catalysts, including transition metal oxides (TMOs),[13] metal–organic frameworks (MOFs),[14] transition metal sulfides (TMSs),[15] and

[a]*Energy Materials Laboratory (EML), Physics Department, School of Sciences and Engineering, The American University in Cairo, New Cairo 11835, Egypt. E-mail: nageh.allam@aucegypt.edu*

[b]*Chemistry Department, Faculty of Science, Sohag University, Sohag-82524, Egypt*

[c]*Department of Analysis and Evaluation, Egyptian Petroleum Research Institute, Cairo, 11727, Egypt*

transition metal phosphides (MPs).[16] Although many of these materials exhibit encouraging catalytic activity, their practical implementation is often hindered by inherent drawbacks such as poor electrical conductivity, limited electrochemical stability, and insufficient mechanistic understanding of active sites.[17,18] Among these candidates, layered double hydroxides (LDHs) have emerged as particularly attractive OER electrocatalysts due to their tunable metal composition, adjustable electronic structure, and distinctive two-dimensional layered architecture.[19,20] The structural versatility of LDHs enables precise modulation of catalytic active sites and offers multiple pathways to enhance OER activity through compositional and morphological engineering.[21–23]

Nevertheless, pristine LDHs suffer from several intrinsic limitations, including low electrical conductivity, sluggish charge-transfer kinetics, structural instability under prolonged operation, and restricted accessibility of active surface sites.[24–29] To address these challenges, diverse strategies, such as heteroatom doping, interface engineering, defect modulation, and hybridization with conductive substrates, have been proposed. Recently, selenium incorporation into NiFe-LDH has emerged as a promising strategy to enhance OER performance by modulating electronic structure and improving charge-transfer kinetics. For instance, Liu *et al.*[30] reported a partial selenization strategy to construct $Ni_{0.85}Fe_{0.15}Se$@LDH/NF heterostructures, achieving an overpotential of 190 mV at 10 mA cm^{-2}. Similarly, Yu *et al.*[31] developed a $FeNi_2Se_4$–FeNi LDH heterointerface with strong electronic interaction that optimizes electron redistribution, delivering 205 mV at 10 mA cm^{-2}. Duan *et al.* further showed that elemental selenium doping promotes the generation of OER-active γ-NiOOH, achieving 200 mV at 10 mA cm^{-2}.[32]

Despite these advances, most reported Se-modified LDHs are synthesized as powders or on macro-porous foams, which still face challenges regarding interfacial contact resistance and mechanical peeling of the active phase under high gas pressure. A critical need remains for monolithic architectures where the electrocatalyst is an intrinsic extension of the conductive substrate.[33,34] In this regard, a top-down fabrication strategy, using ultrathin (0.02 mm) Invar36 alloy sheets, is introduced, diverging from traditional coating methods. By combining controlled electrochemical anodization with subsequent hydrothermal selenization, a self-supported, hierarchical electrode is created, in which FeNi-LDH is rooted directly into the metal bulk. This architecture provides a binder-free path for electron transport and exceptional structural durability during prolonged operation at high current densities, a feature often missing in literature reports of Se-modified LDH powders.[31,35,36]

Despite these advances, issues related to long-term durability, binder-limited charge transport, and scalable synthesis persist. To address these challenges, herein, ultrathin FeNi alloy substrates were first anodized for varying durations (0.5, 1.0, and 1.5 h) to generate a porous FeNi-LDH architecture with abundant exposed active sites. Among these, FeNi-LDH1 (1 h anodization) exhibited the optimal balance between structural integrity and catalytic activity, delivering an overpotential of 270 mV at 10 mA cm^{-2} in 1.0 M KOH. Selenium species were then incorporated *via* hydrothermal treatment using different precursor concentrations (0.03, 0.05, 0.07, and 0.09 M) to tailor the electronic structure and surface chemistry. The optimized FeNi-LDH1-Se_{05} catalyst achieved an overpotential as low as 240 mV at 10 mA cm^{-2}, outperforming commercial benchmarks such as IrO_2 and RuO_2.[37,38] The superior OER performance is attributed to synergistic effects of selenium incorporation: enhanced electrical conductivity, accelerated charge-transfer kinetics, and increased density of accessible active sites. Collectively, these results demonstrate that selenium-engineered, self-supported FeNi-LDH architectures offer an effective and economically viable pathway toward next-generation OER electrocatalysts for sustainable hydrogen production.

2 Experimental section

2.1 Materials and chemicals

Ultrathin $FeNi_{36}$ alloy sheets (Invar36, thickness 0.02 mm) were purchased from Schlenk Company. All chemicals were used as received without further purification. Ethylene glycol (analytical grade, SABIC), ammonium fluoride (NH_4F, 96%, Alfa Aesar), selenium powder (Se, 99.9%, DOP), sodium borohydride ($NaBH_4$, 97.0%, Loba Chemie), potassium hydroxide (KOH, 85.0%, Sigma-Aldrich), hydrazine hydrate (N_2H_4 H_2O, 99%, CDH), and deionized (DI) water were used in all experiments.

2.2 Preparation of the electrode

The FeNi-LDH-based electrocatalysts were synthesized *via* a two-step process, as illustrated in Scheme 1. First, the microporous FeNi-LDH catalysts were prepared through anodization. $FeNi_{36}$ sheets were cut into 1 cm × 2 cm pieces and cleaned sequentially in acetone, ethanol, and DI water for 5 min each under ultrasonication to remove surface impurities and oxides. Anodization was carried out following a modified literature method.[39] The cleaned FeNi sheets were immersed in a 100 mL ethylene glycol electrolyte containing 0.54 M NH_4F and 2.5 M H_2O and anodized at 10 V for 0.5, 1.0, or 1.5 h under gentle stirring to remove gas bubbles forming at the surface. A two-electrode setup was employed with a platinum counter electrode, maintaining an interelectrode distance of approximately 2 cm. After anodization, the samples were rinsed thoroughly with DI water and dried in an oven at 60 °C for 1 h. The resulting samples were labeled according to anodization time as FeNi, FeNi-LDH0.5, FeNi-LDH1, and FeNi-LDH1.5. This was followed by selenization.[40] Selenium precursor solutions were prepared by dissolving Se powder (0.03, 0.05, 0.07, or 0.09 M) and 0.07 M $NaBH_4$ in a mixture of 5 mL N_2H_4 H_2O and 50 mL DI water. The solution was stirred vigorously for 60 min to yield a light red solution. The FeNi-LDH1 sample was then immersed in the prepared solution inside a 100 mL Teflon-lined autoclave, which was sealed and heated at 130 °C for 12 h. After naturally cooling to room temperature, the sample was removed, thoroughly washed with DI water to remove residual selenium species and by-products, and dried in an oven at 60 °C for 1 h. The resulting selenized samples were labeled according to

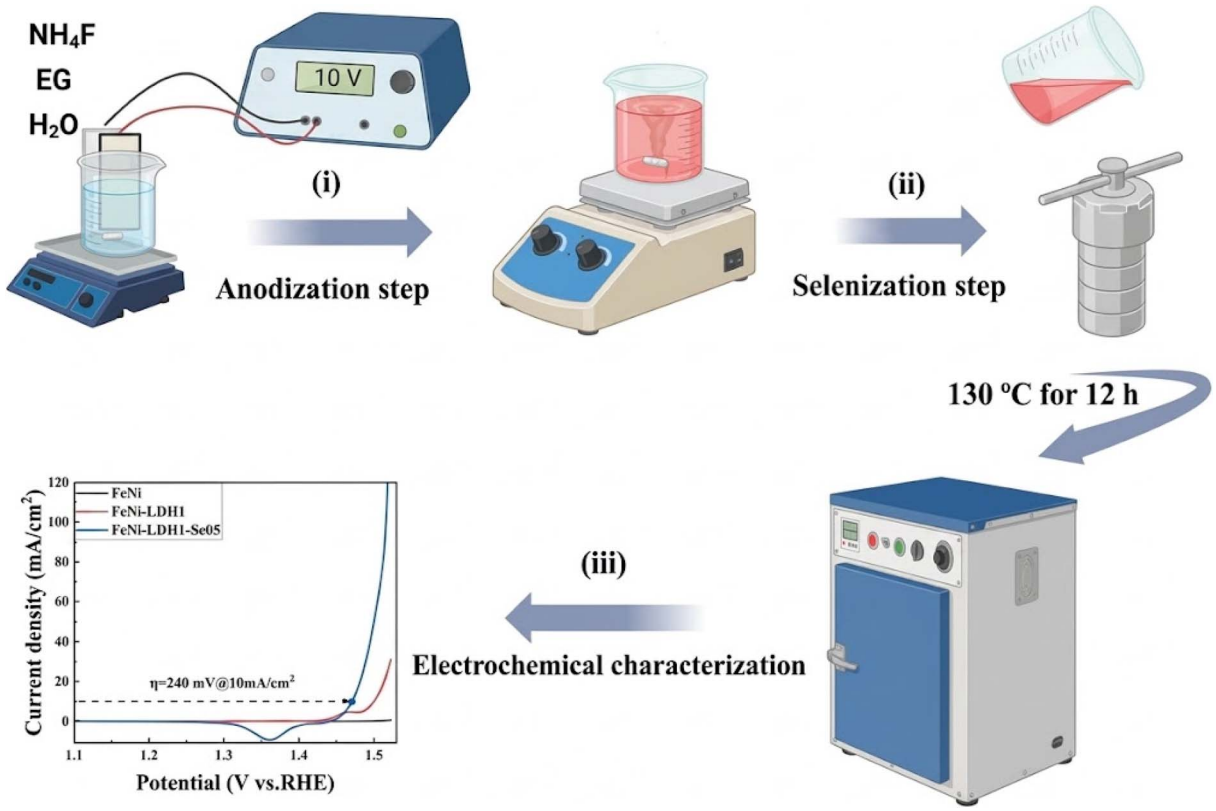

Scheme 1 Illustration of the preparation of the FeNi-LDH1-Se_{05} electrocatalyst *via* a two-step process: (i) electrochemical anodization of ultrathin $FeNi_{36}$ alloy to form a porous FeNi-LDH structure, (ii) hydrothermal selenization to incorporate selenium species, and (iii) subsequent electrochemical characterization of the resulting catalyst.

selenium concentration as FeNi-LDH1-Se03, FeNi-LDH1-Se_{05}, FeNi-LDH1-Se07, and FeNi-LDH1-Se09.

2.3 Preparation of RuO_2 electrode

A 10 mg amount of commercial RuO_2 powder was dispersed in isopropanol (2 mL) and sonicated for 25 min. Then, 25 μL of Nafion solution was added. Additional sonication for 5 min was needed to form a relatively homogeneous suspension. Afterward, the catalyst ink was loaded on the graphite sheet and was ready for testing.

2.4 Materials characterization

The morphology of the samples was examined using a Zeiss Ultra 60 field-emission scanning electron microscope (FESEM) operated at an accelerating voltage of 4 kV. Elemental composition was analyzed *via* energy-dispersive X-ray spectroscopy (EDX) using a JEOL JCM-6000 PLUS system. The crystal structure of the synthesized films was determined by glancing-angle X-ray diffraction (GAXRD) using a PANalytical Empyrean diffractometer equipped with Cu Kα radiation (λ = 1.54 Å), a step size of 0.06°, and a 2θ range of 5–80°. Raman spectra were collected with a 785 nm laser over a spectral range of 100–3200 cm^{-1}. Attenuated total reflection Fourier-transform infrared (ATR-FTIR) measurements were conducted using a Platinum ATR-QL unit with a diamond crystal. The surface composition and chemical states were analyzed by X-ray photoelectron spectroscopy (XPS, Thermo Scientific), with binding energies calibrated to the C 1s peak at 284.8 eV.

2.5 Electrochemical measurements

All electrochemical OER tests were performed in a standard three-electrode configuration using a SP-300 Biologic potentiostat at room temperature. The working electrode was the modified $FeNi_{36}$ sample with a geometric area of 1 cm^2, the counter electrode was a graphite rod, and the reference electrode was Hg/HgO. Experiments were conducted in 1.0 M KOH electrolyte. All potentials were converted to the reversible hydrogen electrode (RHE) scale according to the Nernst equation:

$$E(\text{RHE}) = E\,(\text{Hg/Hg O}) + 0.098 + 0.0591 \times \text{pH} \quad (1)$$

The OER activity was evaluated using linear sweep voltammetry (LSV) at a scan rate of 5 mV s^{-1}. The overpotential (η) was calculated as the difference between the measured potential at 10 mA cm^{-2} and the thermodynamic OER potential (1.23 V *vs.* RHE):

$$\eta = E(\text{OER in RHE@10 mA cm}^{-2}) - 1.23\ (\text{V}) \quad (2)$$

All measurements were *IR*-compensated to account for the solution resistance.

Tafel slopes were derived from LSV curves using:

$$\eta = a + b \log j \quad (3)$$

where η is the overpotential (V), j is the current density (mA cm^{-2}), and b is the Tafel slope (mV dec^{-1}), which provides insight into the kinetics of the OER.

Electrochemical impedance spectroscopy (EIS) measurements were performed at 1.52 V *vs.* RHE over a frequency range of 0.1 Hz to 10^5 Hz to evaluate solution and charge-transfer resistances. The electrochemical double-layer capacitance (C_{dl}) was determined from cyclic voltammetry (CV) in a potential window of 0.1 V centered at the open-circuit voltage at scan rates of 20, 40, 50, 70, and 100 mV s^{-1}:

$$\frac{\Delta(i_a - i_b)}{2} = vC_{dl} \quad (4)$$

where i_a and i_c are the anodic and cathodic currents (mA cm^{-2}), v is the scan rate (mV s^{-1}), and C_{dl} (F) is extracted from the slope of the current *vs.* scan rate plot. The electrochemically active surface area (ECSA) was calculated using eqn (5), assuming a specific capacitance (C_s) of 40 μ F cm^{-2}.[41]

$$\text{ESCA} = \frac{C_{dl}}{C_s} \quad (5)$$

Long-term stability was evaluated *via* chronopotentiometry (CP) at 100 mA cm^{-2} for 120 h (5 days). Faradaic efficiency (FE) was determined using a two-electrode electrolyzer *via* the water-displacement method with a platinum mesh counter electrode in 1.0 M KOH. Chronopotentiometric measurements were performed at 100 mA cm^{-2} for 100 min. The theoretical and experimental moles of oxygen were calculated as followsexperi

2.6 Theoretical oxygen production

The number of electrons used = Q/F, where F is the Faraday constant, and Q is the charge applied at a certain time. Four electrons are required to produce one mole of O_2. Therefore, the number of O_2 moles produced (n) = (number of electrons)/4.

2.7 Experimental oxygen production

The number of O_2 moles produced (n) = displaced water volume (L)/22.4. Consequently, the faradaic efficiency was calculated using eqn (6):

$$\text{FE}(\%) = \frac{\text{number of moles of } O_2 \text{ produced experimentally}}{\text{number of moles of } O_2 \text{ produced theoretically}} \times 100 \quad (6)$$

2.8 Computational methods

Spin-polarized DFT simulations were conducted using VASP 5.4. to determine the optimized geometries and total energies of $FeNi_{36}$, FeNi-LDH1, and FeNi-LDH1-Se_{05} structures. To construct the 64-atom supercell, the Special Quasirandom Structures (SQS) method was employed using the Alloy-Theoretic Automated Toolkit (ATAT) Monte Carlo mcsqs method with the SimplySQS interface.[42,43] The resulting supercell has a composition of $Fe_{0.64}Ni_{0.36}$, containing 41 Fe atoms and 23 Ni atoms, with an experimental equilibrium lattice parameter of 3.5957 Å and atomic volume of 11.62 $Å^3$. The interactions between core and valence electrons were addressed utilizing the projector augmented wave (PAW) method, while the exchange-correlation energy was characterized inside the generalized gradient approximation (GGA) employing the Perdew–Burke–Ernzerhof (PBE) functional. The Kohn–Sham single-electron wave functions were represented using plane waves with an energy cutoff of 500 eV. The convergence requirements for total electronic energy and geometry optimization were established at 10^{-6} eV and 0.01 eV $Å^{-1}$, respectively. To accurately describe the localized 3d states of Ni and Fe, the rotationally invariant Hubbard U correction (DFT+U) was applied following Dudarev *et al.*,[44] with U–J values of 6.6 eV for Ni 3d and 3.5 eV for Fe 3d, as reported in previous studies.[45] A vacuum layer of 15 Å was added to avoid spurious interactions between periodic images. The Gibbs free energy (ΔG) for each elementary reaction step was calculated as:[46,47]

$$\Delta G = \Delta E + \Delta E_{ZPE} - T\Delta S \quad (7)$$

where ΔE, ΔZPE, and ΔS are the changes in the energy, zero-point energy, and entropy contribution of the geometry, respectively. At 298.15 K, ΔZPE and ΔS values for H_2O, H_2 and O_2 Molecules are derived from the NIST-JANAF thermodynamic tables, while the intermediates OH*, O*, and HOO* are generated by computing their vibrational frequencies in adsorbed states.[48,49] The Brillouin zone was sampled using the Monkhorst–Pack scheme with 4 × 3 × 3 k-points for the FeNi-LDH structures and 2 × 2 × 2 k-points for the $FeNi_{36}$ systems. Bader charge analysis was performed to quantitatively evaluate the charge distribution and electron transfer behavior in the optimized structures. The charge density obtained from DFT calculations was partitioned using the Bader scheme based on zero-flux surfaces in the charge density, as implemented in the Henkelman group algorithm. A fine FFT grid was employed to ensure accurate charge integration. The resulting Bader charges were used to determine the effective oxidation states of Fe, Ni, and Se atoms and to analyze the electronic redistribution induced by LDH formation and selenium incorporation. Further computational details are provided in the SI.

3 Results and discussion

3.1 Surface morphology and elemental composition

The surface morphology evolution of the prepared electrodes was systematically investigated using scanning electron microscopy (SEM), as presented in Fig. 1. The pristine $FeNi_{36}$ alloy exhibits a relatively smooth and compact surface with no discernible micro- or nanostructural features (Fig. 1a), reflecting the dense metallic nature of the untreated substrate. Such a featureless morphology typically limits the exposure of electrochemically active sites and restricts electrolyte penetration, thereby constraining catalytic performance.

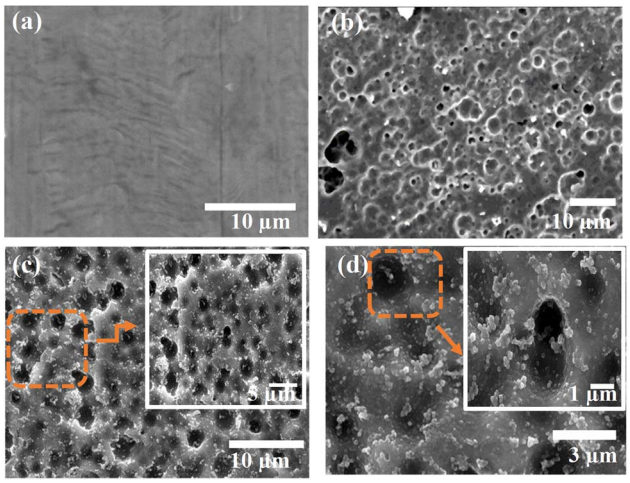

Fig. 1 FESEM images of the electrocatalysts: (a) pristine $FeNi_{36}$ alloy, (b) microporous FeNi-LDH1 formed after anodization, and (c and d) FeNi-LDH1-Se_{05} after selenization at different magnifications.

Following electrochemical anodization, a pronounced transformation in surface morphology is observed. As shown in Fig. 1b, the $FeNi_{36}$ surface evolves into a roughened, microporous architecture composed of interconnected pores and nanoscale features. This anodization-induced restructuring significantly increases the effective surface area and creates abundant open channels, which are highly beneficial for enhancing electrolyte accessibility and facilitating mass transport during OER. More importantly, the formation of this porous FeNi-LDH framework provides a robust scaffold for subsequent surface modification and active site engineering.

After the selenization treatment, the anodized FeNi-LDH surface becomes uniformly decorated with finely dispersed nanoparticles anchored onto the microporous matrix (Fig. 1c and d). The homogeneous distribution of these nanoparticles without noticeable aggregation strongly suggests the successful incorporation of selenium species into the LDH framework. This hierarchical architecture, combining a porous LDH backbone with selenium-modified nanostructures, is expected to promote synergistic effects by simultaneously improving electrical conductivity, exposing additional active sites, and optimizing interfacial charge transfer.

To further elucidate the compositional evolution induced by anodization and selenization, energy-dispersive X-ray spectroscopy (EDX) and elemental mapping analyses were conducted. As shown in Fig. S1a, the pristine $FeNi_{36}$ alloy consists predominantly of Fe (68 wt%) and Ni (31 wt%), confirming the high compositional purity of the Invar36 substrate. After anodization, the oxygen content increases to approximately 6 wt% (Fig. S1b), providing clear evidence for the formation of metal hydroxide/oxide species and the successful generation of the FeNi-LDH phase.

Upon selenization, a substantial compositional change is observed. The oxygen content decreases markedly to about 1 wt% (Fig. S1c), which can be attributed to the strong reducing environment created by sodium borohydride and hydrazine during the hydrothermal process. Concurrently, selenium is incorporated at a high content of 53 wt%, indicating effective surface modification and strong interaction between selenium species and the FeNi-LDH framework. This selenium incorporation is expected to modulate the local electronic structure of the active metal centers, thereby enhancing intrinsic catalytic activity.

3.2 Structural and compositional analysis

The crystal structures of the electrocatalysts were investigated by X-ray diffraction (XRD), as shown in Fig. 2a. The pristine $FeNi_{36}$ (Invar36) alloy exhibits three dominant diffraction peaks at 2θ values of 43.9°, 51.1°, and 75°, corresponding to the (111), (200), and (220) planes of the face-centered cubic (FCC) austenitic Fe–Ni phase (PDF#06-0696). These sharp reflections indicate the high crystallinity and structural integrity of the untreated alloy substrate.

After anodization, significant structural evolution is observed for the FeNi-LDH1 sample (Fig. 2b). Two low-intensity and broadened peaks centered at approximately 15.2° and 22.2° appear, which are assigned to the (003) and (006) planes of NiFe layered double hydroxide (LDH) (PDF#40-0415), reflecting its poor crystallinity and ultrathin layered nature. In addition, a high-intensity diffraction peak at 29.1°, indexed to the (310) plane of β-FeOOH (JCPDS#34-1266), confirms the coexistence of iron oxyhydroxide species within the anodized layer. Such a multiphase structure suggests partial oxidation of the FeNi alloy and the formation of an LDH/oxyhydroxide hybrid surface. Notably, the characteristic FeNi alloy peaks shift from 51.1° and 75° to 50.8° and 74.7° after anodization, respectively. According to Bragg's law, these shifts indicate an increase in interplanar spacing, which can be attributed to lattice strain induced by surface oxidation and hydroxide formation.

Following selenization, the FeNi-LDH1-Se_{05} electrode exhibits new diffraction peaks at 33.3°, 33.8°, 43.3°, 44.4°, and 50.5°, corresponding to the $(\bar{1}\bar{1}2)$, (202), $(\bar{1}\bar{1}4)$, (105), and (310) planes of monoclinic $NiFe_2Se_4$ (JCPDS#01-089-1968),[50] respectively, as shown in Fig. 2b. A magnified XRD view of FeNi-LDH1-Se_{05} in the 31–36° range (Fig. S3) clearly resolves the two reflections at 33.3° and 33.8°. Meanwhile, the characteristic basal reflections of FeNi-LDH1 and β-FeOOH become significantly weakened, indicating partial phase conversion while preserving the layered framework, which remains electrochemically active. Minor peak shifts from 29.1°, 50.8°, and 74.7° to 28.9°, 50.5°, and 74.5°, respectively, are observed after selenization. The shift to lower 2θ angles indicates an increase in interplanar spacing (d) according to Bragg's Law. This lattice expansion can be attributed to the substitution of O^{2-} (1.40 Å) by the larger Se^{2-} (1.98 Å), consistent with prior reports on selenium incorporation into layered double hydroxides where XRD peak shifts confirm successful intercalation without structural destruction.[51–53] Crystallite sizes calculated using the Scherrer equation decrease from 17.9 nm for FeNi-LDH1 to 4.45 nm after selenization, consistent with the formation of finer crystalline domains.

Raman and attenuated total reflection Fourier-transform infrared (ATR-FTIR) spectroscopy were employed to further

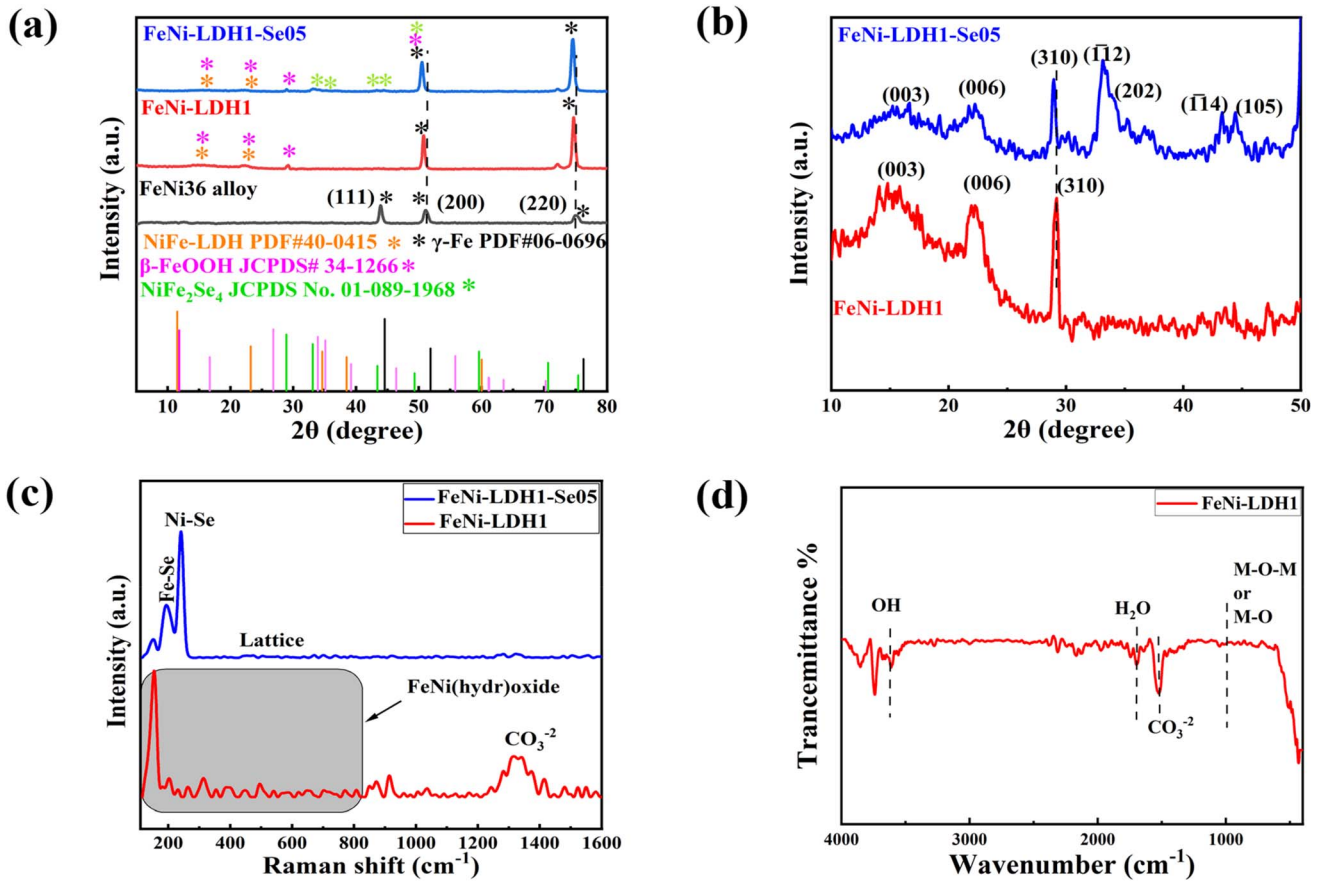

Fig. 2 (a) XRD patterns of pristine $FeNi_{36}$ alloy, FeNi-LDH1, and FeNi-LDH1-$Se_{05}Se_{05}$ catalysts, (b) magnified XRD patterns in the 10–50° 2θ range for FeNi-LDH1 and FeNi-LDH1-Se_{05}, (c) Raman spectra of FeNi-LDH1, and FeNi-LDH1-Se_{05}, and (d) ATR-FTIR spectra of FeNi-LDH1.

probe the structural features and functional groups of the FeNi-LDH-based catalysts (Fig. 2c,d). After anodization, the Raman spectrum of FeNi-LDH1 exhibits several weak and broad features in the 200–720 cm^{-1} region, which can be attributed to mixed Fe–Ni (hydr)oxide or FeNi-LDH phases. In addition, a band at ~1300 cm^{-1} is observed, corresponding to CO_3^{2-} species adsorbed from atmospheric CO_2. The weak intensity and broad nature of these Raman bands indicate that the FeNi (hydr)oxide phase is predominantly amorphous and nanoscale in nature, consistent with the XRD results reported previously.[54] Following selenization, the Raman spectrum of FeNi-LDH1-Se_{05} displays distinct peaks at approximately 210 cm^{-1} (Fe–Se stretching), 275 cm^{-1} (Ni–Se stretching), and 420 cm^{-1} (metal selenide lattice vibrations), confirming the successful formation of ternary FeNi selenide species (Fig. 2c).[55] Notably, the characteristic Raman features of the FeNi (hydr)oxide phase are significantly attenuated after selenization, indicating partial transformation of the original oxide/hydroxide framework.

ATR-FTIR spectra recorded in the range of 500–4000 cm^{-1} (Fig. 2d) display a broad band around 3600 cm^{-1} corresponding to O–H stretching vibrations of surface hydroxyl groups and interlayer water molecules. The band at 1635 cm^{-1} is assigned to the bending vibration of interlayer water (H–O–H), while the band near 1500 cm^{-1} is attributed to the asymmetric stretching of carbonate ions (CO_3^{2-}) absorbed from atmospheric CO_2. Vibrational bands below 800 cm^{-1} arise from M–O and M–O–M lattice vibrations within the layered structure.[56–58]

X-ray photoelectron spectroscopy (XPS) was employed to investigate the surface elemental composition and oxidation states of the FeNi-LDH1-Se_{05} catalyst. The survey spectrum (Fig. S4) reveals the presence of Fe, Ni, Se, and O. Quantitative analysis gives surface atomic percentages of Fe (26.46%), Ni (14.67%), Se (41.81%), and O (17.06%), corresponding to an approximate Fe : Ni : Se : O atomic ratio of 1.0 : 0.55 : .58 : 0.64. The high selenium content confirms successful incorporation of Se into the catalyst surface. The high-resolution Fe 2p spectrum (Fig. 3a) displays a peak at 707.77 eV corresponding to Fe–Se bonding.[60] Peaks at 710.43 eV and 724.13 eV are assigned to Fe^{2+} $2p_{3/2}$ and $2p_{1/2}$, while those at 713.30 eV and 728.09 eV correspond to Fe^{3+} $2p_{3/2}$ and $2p_{1/2}$, indicating the coexistence of Fe^{2+} and Fe^{3+} species.[32] The Ni 2p spectrum (Fig. 3b) exhibits a characteristic peak at 853.5 eV attributed to Ni–Se species.[32,59] Additional peaks at 854.82 eV and 872.44 eV correspond to Ni^{2+} $2p_{3/2}$ and $2p_{1/2}$ in nickel oxide species.[59] The O 1s spectrum (Fig. 3c) can be deconvoluted into three components at 532.3 eV (hydroxyl groups in LDH), 531.0 eV (surface-oxidized oxygen species), and 534.3 eV (adsorbed water).[32,60] The high-resolution Se 3d spectrum (Fig. 3d) displays peaks at 54.3 eV and 55.3 eV corresponding to Se $3d_{5/2}$ and Se $3d_{3/2}$, along with a peak at

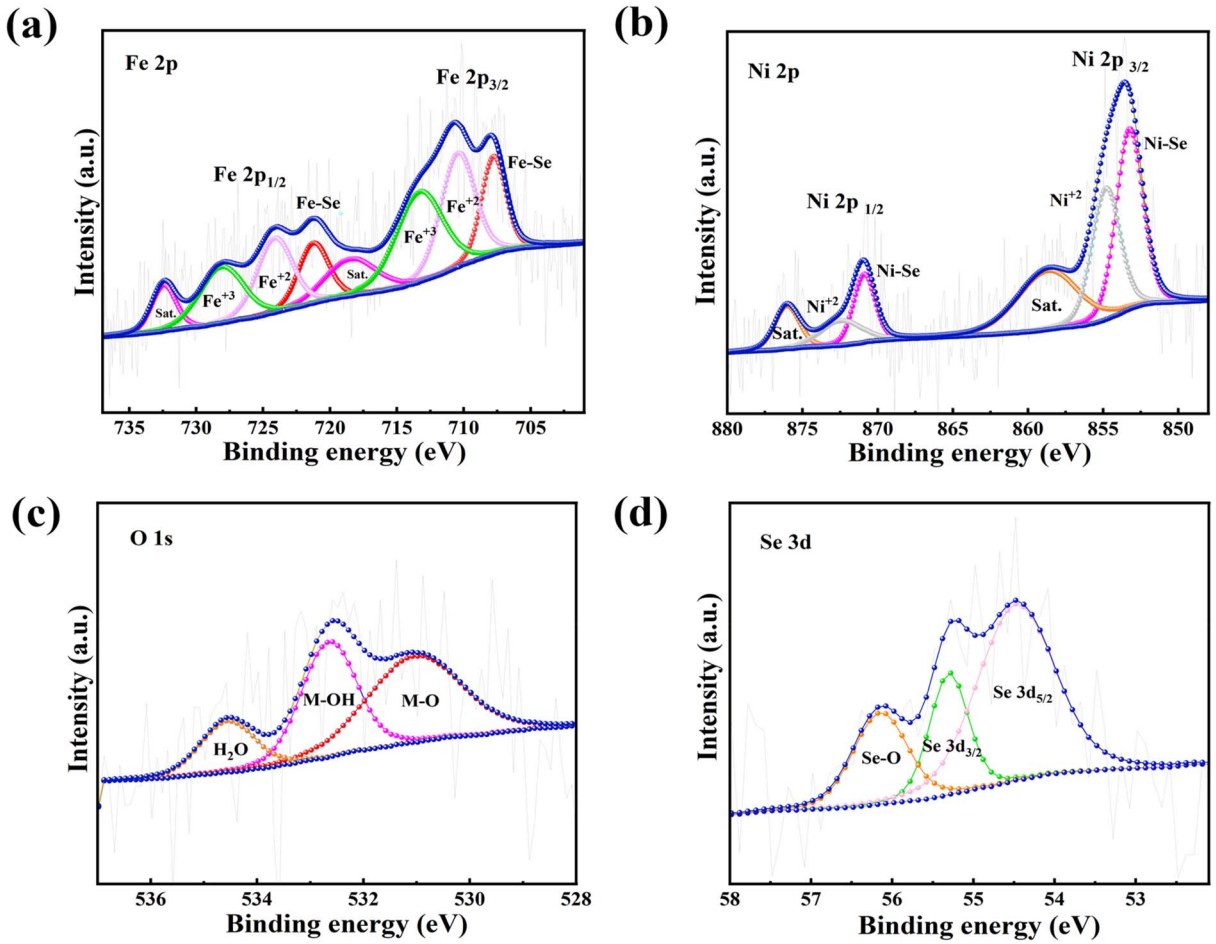

Fig. 3 X-ray photoelectron spectra of the FeNi-LDH1-Se_{05} catalyst: (a) high-resolution Fe 2p spectrum, (b) high-resolution Ni 2p spectrum, (c) O 1s spectrum, and (d) Se 3d spectrum.

56.4 eV attributed to oxidized selenium species (SeO_x) formed due to surface oxidation in air.[61–63]

Overall, the combined XRD, Raman, ATR-FTIR, and XPS analyses confirm the successful incorporation of selenium into the FeNi-LDH-derived framework, the coexistence of mixed-valence Fe and Ni species, and the preservation of layered structural motifs. These structural and compositional features collectively underpin the enhanced electrocatalytic activity and durability of the FeNi-LDH1-Se_{05} catalyst during oxygen evolution.

3.3 Electrochemical performance

The oxygen evolution reaction (OER) activity of the as-prepared catalysts was evaluated in 1.0 M KOH using a standard three-electrode configuration. Linear sweep voltammetry (LSV) measurements were conducted at a scan rate of 5 mV s^{-1} with IR compensation to accurately assess intrinsic catalytic performance. To identify the optimal anodization conditions, *IR*-corrected LSV curves were recorded for FeNi-LDH electrodes anodized for different durations (0.5, 1.0, and 1.5 h), as shown in Fig. S5. The overpotentials required to achieve a current density of 10 mA cm^{-2} were 288, 270, and 271 mV for FeNi-LDH0.5, FeNi-LDH1, and FeNi-LDH1.5, respectively. Among these, FeNi-LDH1 exhibited the lowest overpotential, which is 75 mV lower than that of the pristine $FeNi_{36}$ alloy (345 mV). This pronounced improvement highlights the critical role of anodization in enhancing OER activity by generating a catalytically active FeNi-LDH phase and increasing the density of exposed active sites, consistent with the structural evolution confirmed by XRD.

Subsequent selenization of the optimized FeNi-LDH1 electrode led to a further enhancement in OER performance, as illustrated in Fig. 4a. The FeNi-LDH1-Se_{03}, FeNi-LDH1-Se_{05}, FeNi-LDH1-Se_{07}, and FeNi-LDH1-Se_{09} catalysts required overpotentials of 250, 240, 248, and 255 mV, respectively, to reach 10 mA cm^{-2}. Notably, FeNi-LDH1-Se_{05} delivered the lowest overpotential, representing a 105 mV reduction compared with the pristine $FeNi_{36}$ alloy and a 30 mV decrease relative to FeNi-LDH1. These results clearly demonstrate that the synergistic combination of anodization and selenium incorporation is highly effective in boosting OER activity. By comparison, the monolithic electrode (FeNi-LDH1-Se_{05}) (240 mV) outperforms the commercial RuO_2 (294 mV) at 10 mAcm^{-2} under the same conditions as shown as in Fig. S6. The reaction kinetics was further evaluated through Tafel slope analysis derived from the LSV curves (Fig. 4b). The FeNi, FeNi-LDH1, and FeNi-LDH1-Se_{05}

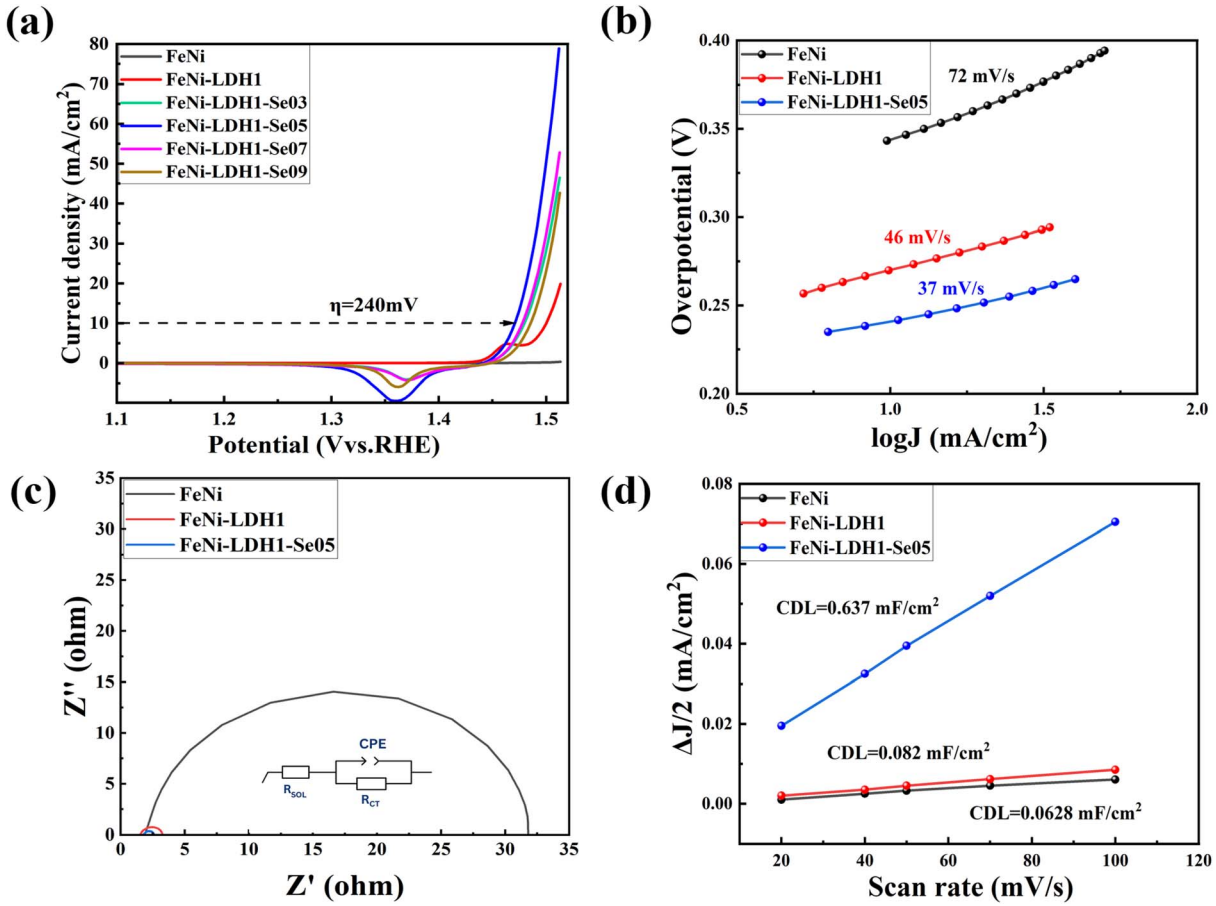

Fig. 4 Electrochemical characterization of FeNi-LDH1-based catalysts: (a) *IR*-corrected linear sweep voltammetry (LSV) curves recorded at a scan rate of 5 mV s^{-1} for FeNi-LDH1 samples selenized with different selenium concentrations; (b) Tafel plots derived from the LSV curves; (c) Nyquist plots obtained from electrochemical impedance spectroscopy (EIS) measured at 1.52 V *versus* RHE over a frequency range of 0.1–10^5 Hz; and (d) double-layer capacitance (C_{dl}) values determined from cyclic voltammetry for FeNi, FeNi-LDH1, and FeNi-LDH1-Se_{05} catalysts.

catalysts exhibit Tafel slopes of 72, 46, and 37 mV dec^{-1}, respectively. The substantially reduced Tafel slope of FeNi-LDH1-Se_{05} indicates faster reaction kinetics and more favorable OER pathways, in excellent agreement with its superior LSV performance.

Electrochemical impedance spectroscopy (EIS) was employed to gain further insight into the charge-transfer characteristics during OER (Fig. 4c). The impedance data were fitted using a Randles-type equivalent circuit incorporating a constant phase element (CPE) to account for surface inhomogeneity, as shown in the inset of Fig. 4c.[64,65] Measurements were conducted at 1.52 V *versus* RHE, where all catalysts exhibited appreciable catalytic currents. The extracted charge-transfer resistance (R_{CT}) values for FeNi, FeNi-LDH1, and FeNi-LDH1-Se_{05} were 30.5, 1.77, and 0.80 Ω, respectively. The markedly lower R_{CT} of FeNi-LDH1-Se_{05} confirms significantly enhanced electron-transfer efficiency and improved electrical conductivity, corroborating the trends observed in the LSV and Tafel analyses.

To further elucidate the origin of the enhanced catalytic activity, the electrochemical surface area (ECSA) was estimated by determining the double-layer capacitance (C_{dl}) from cyclic voltammetry (CV) measurements performed at scan rates of 20, 40, 50, 70, and 100 mV s^{-1} (Fig. S7). As shown in Fig. 4d, the C_{dl} values were determined to be 0.0628, 0.082, and 0.637 mF cm^{-2} for FeNi, FeNi-LDH1, and FeNi-LDH1-Se_{05}, respectively. Using a specific capacitance (C_s) value of 40 μF cm^{-2} [41], the corresponding ECSA values were calculated to be 1.57, 2.05, and 15.93 cm^2, respectively. The substantially larger ECSA of FeNi-LDH1-Se_{05} indicates a significantly higher density of electrochemically accessible active sites, which rationalizes its lower overpotential, accelerated kinetics, and overall superior OER performance.

The FeNi-LDH1-$Se_{05}Se_{05}$ catalyst, which exhibited outstanding OER activity in the three-electrode configuration, was further evaluated in a two-electrode alkaline water electrolyzer to assess its practical applicability. A platinum counter electrode was employed to minimize the hydrogen evolution reaction (HER) overpotential. As shown in the polarization curve (Fig. 5a), the electrolyzer required a low cell voltage of 1.56 V to reach a current density of 10 mA cm^{-2}, demonstrating efficient overall water splitting performance.

The oxygen evolution performance was quantitatively examined using the water displacement method in a two-compartment electrolyzer, in which the cathode and anode chambers were separated by a Nafion membrane. Gas evolution was monitored at a constant current density of 100 mA cm^{-2}

over different time intervals. As depicted in Fig. 5b, the experimentally measured amounts of O_2 closely match the theoretical values calculated as shown previously in experimental section, resulting in a high faradaic efficiency of approximately 97.5%. This close agreement confirms that the applied current is predominantly utilized for oxygen evolution with minimal parasitic reactions.

Long-term operational stability, a critical requirement for practical OER electrocatalysts, was evaluated by chronopotentiometry (CP) at a high current density of 100 mA cm^{-2} for 120 h (5 days) in 1.0 M KOH (Fig. 5c). The FeNi-LDH1-Se_{05} catalyst exhibits excellent durability, maintaining nearly constant OER activity throughout the test with only a slight increase in overpotential of approximately 30 mV. This minimal performance decay highlights the robustness of the catalyst under prolonged anodic polarization.

Post-electrolysis FESEM imaging (Fig. S8) demonstrates that the characteristic microporous morphology of FeNi-LDH1-Se_{05} remains largely intact after prolonged operation under harsh alkaline conditions, confirming excellent structural stability. This was accompanied by an increase in oxygen content to 15 wt% and a decrease in selenium content to 0.48 wt% (Fig. S1d), indicating partial transformation of metal selenide species into electrochemically active (oxy)hydroxide phases. This is further supported by XRD analysis (Fig. S9), which shows only weak residual selenide peaks, confirming partial conversion.

Table 1 ICP-OES results of FeNi-LDH1-Se_{05} before and after the stability at 100 mA cm^{-2} for 5 days

Selenium content after LSV	674 0.5 μg L^{-1}
Selenium content after CP for 5 days@100 mA cm^{-2}	727 μg L^{-1}

Upon anodic polarization, selenium is gradually oxidized and partially leaches into the electrolyte as soluble selenite/selenate (confirmed by ICP-OES, Table 1), while the surface concurrently incorporates oxygen to form an (oxy)hydroxide-rich layer. This *in situ* surface reconstruction is consistent with previously reported behavior of transition-metal chalcogenide-based OER catalysts[66–68] and is often associated with sustained or enhanced catalytic activity. The transformation leaves behind a metastable, defect-rich, and highly active surface that exhibits superior OER activity compared to pristine FeNi-LDH (240 mV *vs.* 270 mV at 10 mA cm^{-2}).

Thus, selenium serves as a sacrificial electronic modulator and structural activator during the initial stages of OER. Specifically, selenization pre-treats the FeNi-LDH framework by inducing electron transfer from Ni to Se, creating lattice strain, and generating defect-rich sites. The role of selenium is

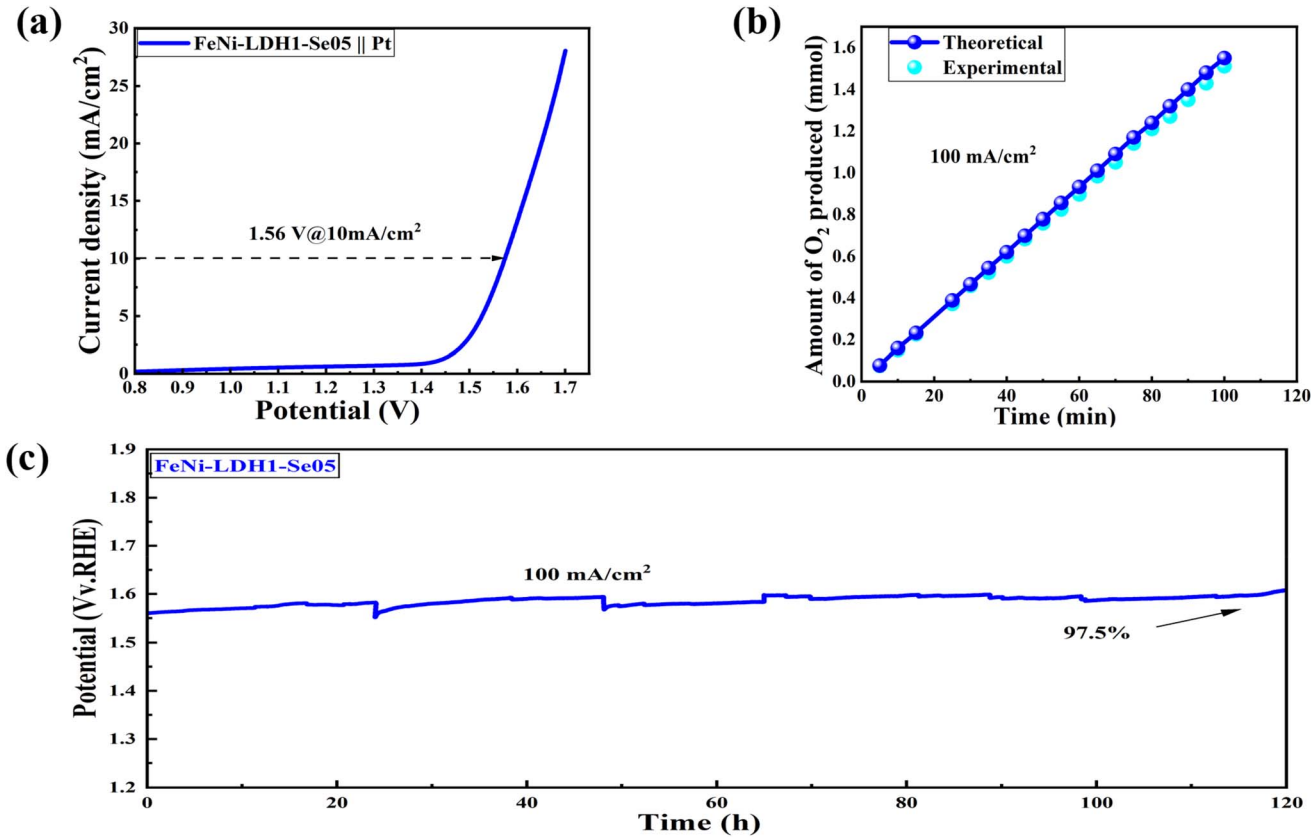

Fig. 5 Electrochemical performance of the FeNi-LDH1-Se_{05} catalyst for overall water splitting in 1.0 M KOH: (a) *IR*-compensated linear sweep voltammetry (LSV) curve recorded at 5 mV s^{-1} using FeNi-LDH1-Se_{05} as the anode and Pt as the cathode; (b) experimentally measured and theoretically calculated O_2 evolution *versus* time at a constant current density of 100 mA cm^{-2}; (c) chronopotentiometry (CP) profile of FeNi-LDH1-Se_{05} at 100 mA cm^{-2} over 120 h to evaluate long-term stability.

therefore not as a permanent active site but as a transient electronic and structural promoter that enables a more active reconstructed surface. This sacrificial activator mechanism is consistent with prior reports on transition metal chalcogenides for OER.

Overall, FeNi-LDH1-Se_{05} preserves its hierarchical structure, compositional homogeneity, and partial selenium content under harsh OER conditions. These features, combined with surface reconstruction, underscore the catalyst's structural and electrochemical robustness, highlighting its practical viability for long-term alkaline water oxidation. A comparative summary of OER overpotentials measured in 1.0 M KOH for FeNi-LDH1-Se_{05} and other reported surface-modified FeNi-LDH-based catalysts is illustrated in Fig. 6 and listed in Table S1. The comparison clearly highlights the superior catalytic performance of FeNi-LDH1-Se_{05} as a non-precious-metal OER catalyst, outperforming many state-of-the-art FeNi-LDH derivatives reported to date.

To elucidate the fundamental origin of the enhanced OER kinetics, the atomic structures of $FeNi_{36}$, FeNi-LDH1, and FeNi-LDH1-Se_{05} were constructed and fully optimized, as shown in Fig. 7a–c, and subsequently employed for density functional theory (DFT) calculations. The calculated Gibbs free energy diagrams for the oxygen evolution reaction on these three catalysts are presented in Fig. 6d. For all models, the OER proceeds through the conventional four-step proton-coupled electron transfer mechanism involving the formation of HO*, O*, and HOO* intermediates.

For each catalyst, the reaction pathway initiates from adsorbed H_2O, which is taken as the reference state ($\Delta G = 0$ eV). The first elementary step corresponds to water adsorption and deprotonation to form HO*, as illustrated in Fig. 6e. Compared with metallic $FeNi_{36}$, both FeNi-LDH1 and FeNi-LDH1-Se_{05} exhibit moderated HO* adsorption energies, effectively avoiding the excessively strong binding observed on $FeNi_{36}$. Such overly strong HO* adsorption on $FeNi_{36}$ is detrimental, as it impedes subsequent reaction steps and slows overall OER kinetics.

The second step involves the transformation of HO* to O*. On $FeNi_{36}$, the O* intermediate is excessively stabilized, resulting in a deep energy minimum. While strong O* binding can facilitate O–H bond cleavage, it introduces a large energetic penalty for subsequent oxidation to HOO*. In contrast, FeNi-LDH1 displays weakened O* adsorption, reflecting a more favorable balance between adsorption strength and surface reactivity. Notably, selenium incorporation further fine-tunes the O* binding energy, yielding a thermodynamically optimized intermediate configuration.

The third step, corresponding to the formation of the HOO* intermediate, is identified as the rate-determining step (RDS) for all three catalysts, as it exhibits the highest Gibbs free energy change (ΔG_3). $FeNi_{36}$ shows the largest ΔG_3 value of 1.51 eV, indicating sluggish OER kinetics and a high theoretical overpotential. Upon transformation to the layered double hydroxide structure, ΔG_3 decreases to 1.49 eV, signifying improved catalytic activity. Importantly, selenium doping leads to a further reduction in ΔG_3 to 1.37 eV, demonstrating that selenium incorporation effectively promotes O–O bond formation and lowers the energy barrier of the potential-determining step. The final step, involving O_2 desorption and regeneration of the active site, is energetically less demanding than the RDS for all catalysts. Accordingly, the overall ΔG_{max} follows the trend: $FeNi_{36}$ > FeNi-LDH1 > FeNi-LDH1-Se_{05}.

This theoretical trend is in excellent agreement with the experimentally observed OER performance, where FeNi-LDH1-Se_{05} exhibits the lowest overpotential and fastest reaction kinetics. The enhanced activity of FeNi-LDH1-Se_{05} arises from the synergistic effects of LDH structural reconstruction and selenium incorporation, which collectively optimize the adsorption energies of key reaction intermediates, reduce the energy barrier of the rate-determining step, and bring the catalyst closer to the ideal thermodynamic pathway for OER.

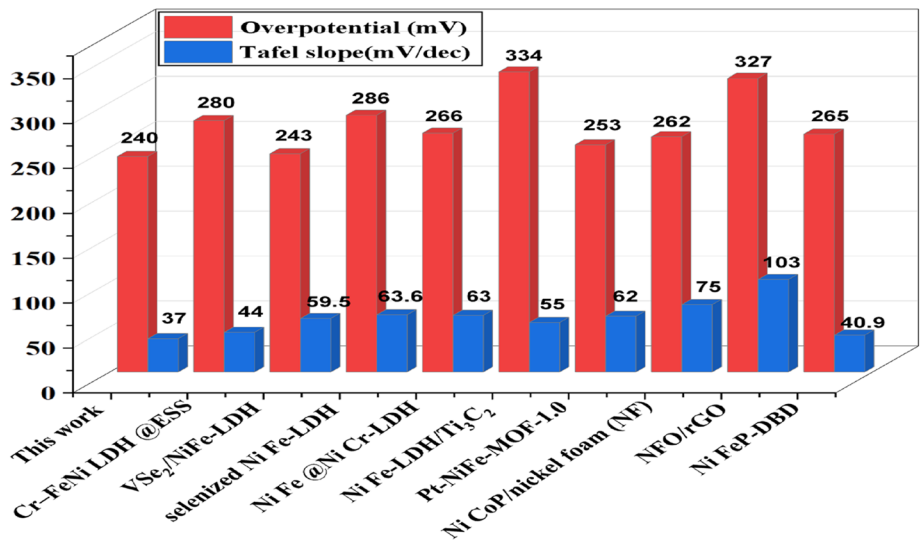

Fig. 6 3-D histogram comparing the performance of FeNi-LDH1-Se_{05} with different FeNi-based catalysts using the overpotential @10 mA cm^{-2} and Tafel slope values.

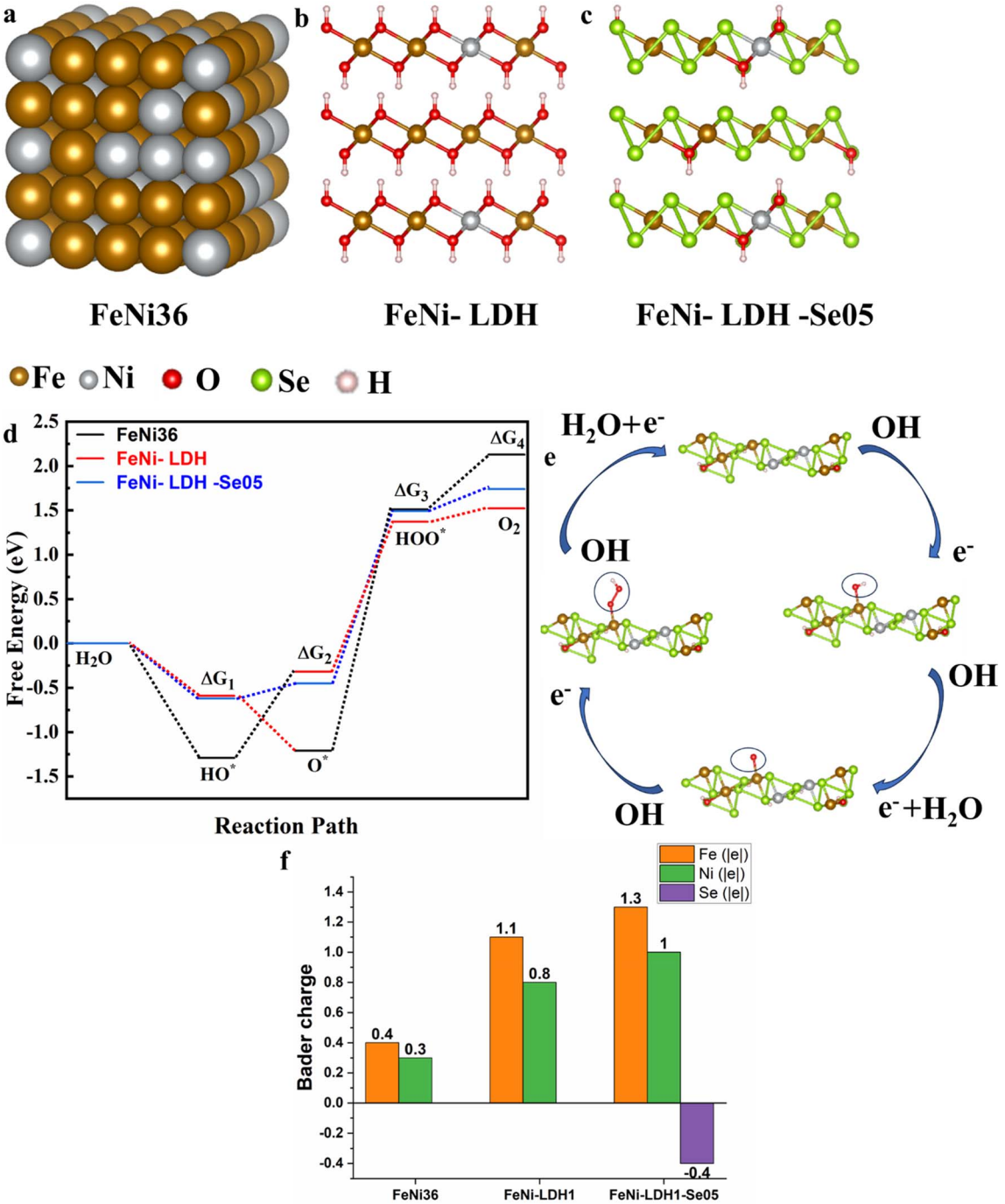

Fig. 7 (a–c) Optimized geometries of $FeNi_{36}$, FeNi-LDH1, and Se-doped FeNi-LDH (FeNi-LDH1-Se_{05}), respectively, (d) Gibbs free energy profiles for the four-step oxygen evolution reaction (OER) pathway on $FeNi_{36}$, FeNi-LDH, and FeNi-LDH-Se_{05} catalysts, (e) schematic illustration of the OER reaction mechanism, highlighting the formation of HO*, O*, and HOO* intermediates, and (f) Bader charge of Fe, Ni, and Se atoms in $FeNi_{36}$, FeNi-LDH1, and FeNi-LDH-Se_{05}.

To quantitatively elucidate the electronic origin of the optimized OER activity, Bader charge analysis was performed based on the quantum theory of atoms in molecules (QTAIM) framework, which partitions the total electron density into non-overlapping atomic volumes bounded by zero-flux surfaces. This method provides a basis set independent measure of net atomic charges, enabling direct comparison of oxidation states across structurally distinct catalyst models. The computed Bader charges are summarized in Table 2. In metallic $FeNi_{36}$, Fe and Ni atoms exhibit weak charge polarization, with average Bader charges of approximately $+0.4|e|$ for Fe and $+0.3|e|$ for Ni. This electronic configuration is consistent with strong metallic bonding and overly strong adsorption of oxygenated intermediates, as reflected by the deep ΔG(HO*) and ΔG(O*) minima in Fig. 6d. Upon transformation into FeNi-LDH1, coordination with hydroxyl ligands induces significant electron withdrawal

Table 2 Bader charge analysis of Fe, Ni, and Se atoms in $FeNi_{36}$, FeNi-LDH1, and FeNi-LDH1-Se_{05}

Catalyst	Fe ($\|e\|$)	Ni ($\|e\|$)	Se ($\|e\|$)
$FeNi_{36}$	+0.4	+0.3	—
FeNi-LDH1	+1.1	+0.8	—
FeNi-LDH1-Se_{05}	+1.3	+1.0	−0.4

from the metal centers, increasing the Bader charges to approximately +1.1$|e|$ for Fe and +0.8 $e|$ for Ni. This moderated oxidation state weakens O* binding and stabilizes the HO* and HOO* intermediates, leading to a more balanced free-energy landscape.

Following selenium doping, pronounced charge redistribution occurs. Selenium atoms gain electrons, exhibiting Bader charges of approximately −0.4$|e|$, while adjacent Fe and Ni atoms become further oxidized to +1.3$|e|$ and +1.0$|e|$, respectively. This enhanced charge polarization effectively suppresses excessive O* binding while simultaneously stabilizing the HOO* intermediate, resulting in a reduced ΔG(O* → HOO*) gap and a lowered potential-determining step. Consequently, Se-doped FeNi-LDH1 exhibits the most favorable OER thermodynamics among the three catalysts, consistent with its lowest ΔG_3 value and superior experimental performance.

4 Conclusion

A simple and effective strategy was developed to fabricate a self-supported FeNi-LDH1-Se_{05} electrocatalyst by combining anodization with hydrothermal selenization. This method produces a highly efficient OER catalyst under alkaline conditions. The optimized electrode delivers an overpotential of 240 mV at 10 mA cm^{-2}, a Tafel slope of 37 mV dec^{-1}, and a charge transfer resistance of only 0.8 Ω indicating fast kinetics and excellent electron transport. The electrode also exhibits remarkable long-term durability, operating steadily at 100 mA cm^{-2} for 120 hours (5 days). During this extended test, the porous structure remains largely intact, while the surface gradually transforms from metal selenides into active (oxy) hydroxide species. The high catalytic activity stems from a synergistic combination of factors: improved conductivity, increased accessible active surface area, the formation of the FeNi-LDH phase, and electronic modulation induced by selenium incorporation. A key strength of this monolithic electrode is its binder-free design, which eliminates polymer-related issues and ensures full accessibility of selenium-modified active sites. To further validate practical potential, this electrode requires evaluation in a real zero-gap electrolyzer under more industrial conditions. In addition, a comprehensive life-cycle and techno-economic analysis is necessary to determine whether this earth-abundant catalyst offers genuine cost and overall benefit advantages over noble-metal counterparts. Addressing these remaining limitations would position FeNi-LDH1-Se_{05} as a strong candidate for real-world water splitting, advancing sustainable energy technologies. Overall, this work provides insight into the interplay between structure, electronics, and activity in OER catalysis, while offering a straightforward route to high-performance, non-precious-metal electrocatalysts.

Conflicts of interest

The authors declare no competing financial interest.

Data availability

The data supporting this article have been included as part of the supplementary information (SI). Supplementary information is available. See DOI: https://doi.org/10.1039/d6ra02304e.

Acknowledgements

The financial support of this work by the African Engineering and Technology Network (AFRETEC) is highly appreciated.

Notes and references

1 P. J. Megía, A. J. Vizcaíno, J. A. Calles and A. Carrero, *Energy Fuels*, 2021, **35**, 16403–16415.
2 S. M. Fawzy, M. K. M. Ali and N. K. Allam, *ACS Sustainable Chem. Eng.*, 2026, **14**, 4745–4761.
3 A. Mehtab, S. A. Ali, I. Sadiq, S. Shaheen, H. Khan, M. Fazil, N. A. Pandit, F. Naaz and T. Ahmad, *ACS Sustainable Resour. Manage.*, 2024, **1**, 604.
4 M. M. Hasan, G. E. Khedr and N. K. Allam, *ACS Appl. Nano Mater.*, 2022, **5**, 15457–15464.
5 A. Govind Rajan, J. M. P. Martirez and E. A. Carter, *ACS Catal.*, 2020, **10**, 11177–11234.
6 N. K. Awad, E. A. Ashour and N. K. Allam, *J. Renewable Sustainable Energy*, 2014, **6**, 022702.
7 N. M. Deyab, P. Steegstra, A. Hubin, M. P. Delplancke, H. Rahier and N. K. Allam, *J. Power Sources*, 2015, **280**, 339–346.
8 T. Wang, M. Xu, F. Li, Y. Li and W. Chen, *Appl. Catal., B*, 2021, **280**, 119421.
9 K. E. Salem, A. A. Saleh, G. E. Khedr, B. S. Shaheen and N. K. Allam, *Energy Environ. Mater.*, 2023, **6**, e12324.
10 J. Yang, Q. Shao, B. Huang, M. Sun and X. Huang, *iScience*, 2019, **11**, 492–504.
11 A. M. Mohamed, A. S. Aljaber, S. Y. AlQaradawi and N. K. Allam, *Chem. Commun.*, 2015, **51**, 12617–12620.
12 J. Ahn, Y. S. Park, S. Lee, J. Yang, J. Pyo, J. Lee, G. H. Kim, S. M. Choi and S. K. Seol, *Sci. Rep.*, 2022, **12**, 346.
13 H. M. A. Amin, L. Zan and H. Baltruschat, *Surf. Interfaces*, 2024, **54**, 105218.
14 C. Li, H. Zhang, M. Liu, F.-F. Lang and J. Pang, *Ind. Chem. Mater.*, 2023, **1**, 9–38.
15 H. M. A. Amin and U. Apfel, *Eur. J. Inorg. Chem.*, 2020, 2679–2690.
16 A. Nairan, Z. Feng, R. Zheng, U. Khan and J. Gao, *Adv. Mater.*, 2024, **36**, 2401448.
17 W. Xu, Y. Wu, S. Xi, Y. Wang, Y. Wang, Y. Ke, L. Ding, X. Wang, J. Yang, W. Zhang, K. P. Loh, F. Ding and M. Chhowalla, *Nat. Synth.*, 2025, **4**, 327–335.

18 Z. Wang, Y. Liang, T. Fang, X. Song, L. Yang, L. Wen, J. Wang, D. Zhao and S. Wang, *Nanomaterials*, 2025, **15**, 294.
19 L. Feng, A. Li, Y. Li, J. Liu, L. Wang, L. Huang, Y. Wang and X. Ge, *ChemPlusChem*, 2017, **82**, 483–488.
20 X. Guo, F. Zhang, D. G. Evans and X. Duan, *Chem. Commun.*, 2010, **46**, 5197.
21 B. M. Hunter, W. Hieringer, J. R. Winkler, H. B. Gray and A. M. Müller, *Energy Environ. Sci.*, 2016, **9**, 1734–1743.
22 X. Jia, S. Gao, T. Liu, D. Li, P. Tang and Y. Feng, *Electrochim. Acta*, 2017, **245**, 59–68.
23 Y. Xu, Y. Hao, G. Zhang, Z. Lu, S. Han, Y. Li and X. Sun, *RSC Adv.*, 2015, **5**, 55131–55135.
24 C. Wan, J. Jin, X. Wei, S. Chen, Y. Zhang, T. Zhu and H. Qu, *J. Mater. Sci. Technol.*, 2022, **124**, 102–108.
25 S.-W. Wu, S.-Q. Liu, X.-H. Tan, W.-Y. Zhang, K. Cadien and Z. Li, *Chem. Eng. J.*, 2022, **442**, 136105.
26 P. Xiong, X. Zhang, H. Wan, S. Wang, Y. Zhao, J. Zhang, D. Zhou, W. Gao, R. Ma, T. Sasaki and G. Wang, *Nano Lett.*, 2019, **19**, 4518–4526.
27 R. Zhang, Y. Han, Q. Wu, M. Lu, G. Liu, Z. Guo, Y. Zhang, J. Zeng, X. Wu, D. Zhang, L. Wu, N. Song, P. Yuan, A. Du, K. Huang, J. Chen and X. Yao, *Small*, 2024, **20**, 2402397.
28 B. Wu, S. Gong, Y. Lin, T. Li, A. Chen, M. Zhao, Q. Zhang and L. Chen, *Adv. Mater.*, 2022, **34**, 2108619.
29 Z. Zhang, C. Wang, X. Ma, F. Liu, H. Xiao, J. Zhang, Z. Lin and Z. Hao, *Small*, 2021, **17**, 2103785.
30 S. Liu, Y. Ma, Z. Wang, J. Guo, L. Shi and X. Ma, *Appl. Surf. Sci.*, 2026, **718**, 164897.
31 H. Yu, Y. Xie, L. Deng, H. Huang, J. Song, D. Yu, L. Li and S. Peng, *Inorg. Chem. Front.*, 2022, **9**, 146–154.
32 S. Duan, S. Chen, T. Wang, S. Li, J. Liu, J. Liang, H. Xie, J. Han, S. Jiao, R. Cao, H.-L. Wang and Q. Li, *Nanoscale*, 2019, **11**, 17376–17383.
33 K. Xu, H. Zhong, X. Li, J. Song, L. A. Estudillo-Wong, J. Yang, Y. Feng, X. Zhao and N. Alonso-Vante, *Small Sci.*, 2024, **4**, 2300294.
34 P. Byaruhanga, M. Haroon Khan, L. Yu, Y. Wang and S. Chen, *ECS Meet. Abstr.*, 2025, 1416.
35 S. Zhu, Z. Cui, Z. Li, S. Wu, M. Guo, H. Jiang and Y. Liang, *Sustain. Energy Fuels*, 2021, **5**, 3205–3212.
36 X.-S. Gong, X. Liu and J. Zhou, *Nanoscale*, 2025, **17**, 5301–5315.
37 J. Zhao, S. Chen, Z. Zhang, X. Song, Y. Wang, J. Xiong and Y. Zhao, *Appl. Catal. Gen.*, 2026, **711**, 120733.
38 R. Jiang, D. T. Tran, J. Li and D. Chu, *Energy Environ. Mater.*, 2019, **2**, 201–208.
39 Z. Xu, D. Quintero, S. Kitano, T. Nagao, M. Iwai, Y. Aoki, K. Fushimi and H. Habazaki, *Electrochim. Acta*, 2024, **491**, 144352.
40 S. A. Teama, H. M. El Sharkawy and N. K. Allam, *Energy Fuels*, 2023, **37**, 7468–7478.
41 J. Wang, Z. Li, L. Feng, D. Lu, W. Fang, Q. Zhang, D. Hedman and S. Tong, *J. Colloid Interface Sci.*, 2025, **677**, 976–985.
42 A. Van De Walle, P. Tiwary, M. De Jong, D. L. Olmsted, M. Asta, A. Dick, D. Shin, Y. Wang, L.-Q. Chen and Z.-K. Liu, *Calphad*, 2013, **42**, 13–18.
43 M. Lebeda, J. Drahokoupil, P. Vlčák, Š. Svoboda and A. van de Walle, *arXiv*, 2025, vol. **2510**, p. , p. 18020.
44 S. L. Dudarev, G. A. Botton, S. Y. Savrasov, C. J. Humphreys and A. P. Sutton, *Phys. Rev. B*, 1998, **57**, 1505–1509.
45 D. Friebel, M. W. Louie, M. Bajdich, K. E. Sanwald, Y. Cai, A. M. Wise, M.-J. Cheng, D. Sokaras, T.-C. Weng, R. Alonso-Mori, R. C. Davis, J. R. Bargar, J. K. Nørskov, A. Nilsson and A. T. Bell, *J. Am. Chem. Soc.*, 2015, **137**, 1305–1313.
46 S. Gamal, G. E. Khedr, M. Nashaat, L. M. Salah, A. A. Maarouf and N. K. Allam, *Sci. Rep.*, 2025, **15**, 26329.
47 M. M. Abodouh, G. E. Khedr and N. K. Allam, *Int. J. Hydrog. Energy*, 2024, **61**, 922–933.
48 A. Magdy Saad, M. Saad Sayed, S. Alhammadi, G. E. Khedr, J.-J. Shim and W. K. Kim, *Appl. Surf. Sci.*, 2024, **654**, 159415.
49 S. Ismail, G. E. Khedr, F. Z. Salem and N. K. Allam, *Energy Fuels*, 2025, **39**, 13703–13714.
50 J. Wang, F. Wang, B. Qin, Y. Wu, H. Yang, X. Li, L. Wang, X. Qin and X. Xu, *Chin. Chem. Lett.*, 2024, **35**, 109449.
51 R. D. Shannon, *Acta Crystallogr., Sect. A*, 1976, **32**, 751–767.
52 X. Hou and R. J. Kirkpatrick, *Chem. Mater.*, 2000, **12**, 1890–1897.
53 N. Chubar, *J. Mater. Chem. A*, 2014, **2**, 15995–16007.
54 N. Akbari, S. Nandy, K. H. Chae and M. M. Najafpour, *Langmuir*, 2023, **39**, 11807–11818.
55 S. Navazani and F. Torabi, *Sci. Rep.*, 2025, **15**, 35611.
56 F. Zheng, M. A. Gaikwad, Z. Fang, S. Jang and J. H. Kim, *Energy Fuels*, 2024, **38**, 6290–6299.
57 D. Pan, S. Ge, J. Zhao, Q. Shao, L. Guo, X. Zhang, J. Lin, G. Xu and Z. Guo, *Dalton Trans.*, 2018, **47**, 9765–9778.
58 J. Xu, S. Gai, F. He, N. Niu, P. Gao, Y. Chen and P. Yang, *J. Mater. Chem. A*, 2014, **2**, 1022–1031.
59 Y. Guo, Y. Liu, Y. Liu, C. Zhang, K. Jia, J. Su and K. Wang, *Catalysts*, 2022, **12**, 739.
60 J. Dai, Y. Zhang, H. Song and L. Liu, *Int. J. Hydrog. Energy*, 2024, **87**, 130–137.
61 M. Liu, Y.-Y. Sun, Y.-X. Zhu, L.-K. Wu, M.-Y. Jiang, G.-Y. Hou and Y.-P. Tang, *Int. J. Hydrog. Energy*, 2021, **46**, 6427–6440.
62 Y.-Y. Sun, M.-Y. Jiang, L.-K. Wu, G.-Y. Hou, Y.-P. Tang and M. Liu, *Sustain. Energy Fuels*, 2020, **4**, 582–588.
63 A. M. Al-Enizi, S. F. Shaikh, M. Ubaidullah, M. A. Ghanem and R. S. Mane, *Int. J. Hydrog. Energy*, 2020, **45**, 15904–15914.
64 G.-R. Zhang, L.-L. Shen, P. Schmatz, K. Krois and B. J. M. Etzold, *J. Energy Chem.*, 2020, **49**, 153–160.
65 A. K. Gomaa, B. S. Shaheen, G. E. Khedr, A. M. Mokhtar and N. K. Allam, *Energy Fuels*, 2022, **36**, 7025–7034.
66 X. Xu, F. Song and X. Hu, *Nat. Commun.*, 2016, **7**, 12324.
67 Z. Wang, J. Li, X. Tian, X. Wang, Y. Yu, K. A. Owusu, L. He and L. Mai, *ACS Appl. Mater. Interfaces*, 2016, **8**, 19386–19392.
68 J. Zhu, T. Jiang, D. Gerlach, P. Rudolf, V. Kyriakou, D. M. Morales and P. P. Pescarmona, *Int. J. Hydrog. Energy*, 2025, **143**, 235–249.